A&A, 695, A128 (2025)
https://doi.org/10.1051/0004-6361/202451282

Astronomy & Astrophysics

The Compton-thick active galactic nuclei luminosity function in the local Universe

A robust estimate combining Burst Alert Telescope detections and *NuSTAR* spectra

I. Georgantopoulos*, E. Pouliasis, A. Ruiz, and A. Akylas

Institute for Astronomy Astrophysics Space Applications and Remote Sensing (IAASARS), National Observatory of Athens, Ioannou Metaxa & Vasileos Pavlou, Penteli 15236, Greece

Received 27 June 2024 / Accepted 10 December 2024

ABSTRACT

Compton-thick active galactic nuclei (AGN) arguably constitute the most elusive class of sources, as they are absorbed by large column densities above 10^{24} cm^{-2}. These extreme absorptions hamper the detection of the central source even in hard X-ray energies. In this work, we use both *Neil Gehrels Swift* and *NuSTAR* observations to derive the most accurate yet Compton-thick AGN luminosity function. We first compiled a sample of candidate Compton-thick AGN ($N_H = 10^{24-25}$ cm^{-2}) detected in the Swift Burst Alert Telescope (BAT) all-sky survey in the 14–195 keV band. We confirmed that they are Compton-thick sources by using the *NuSTAR* follow-up observations already presented in the literature. Our sample is composed of 44 sources, consistent with a column density of 10^{24}–10^{25} cm^{-2} at the 90% confidence level. These sources have intrinsic luminosities higher than $L_{10-50\,keV} \sim 3 \times 10^{41}$ erg s^{-1} and are found up to a redshift of z = 0.05 (≈200 Mpc). We derived the luminosity function of Compton-thick AGN using a Bayesian methodology where both the full column density and the luminosity distributions are taken into account. The faint end of the luminosity function is flat, having a slope of $\gamma_1 = 0.01^{+0.51}_{-0.74}$, rather arguing against a numerous population of low luminosity Compton-thick AGN. Based on our luminosity function, we estimate that the fraction of Compton-thick AGN relative to the total number of AGN is of the order of 24 ± 5%, which is in agreement with previous estimates in the local Universe based on BAT samples.

Key words. galaxies: active – galaxies: nuclei – quasars: supermassive black holes – galaxies: Seyfert

1. Introduction

Active galactic nuclei (AGN) are among the most luminous sources in the Universe. They are powered by accretion onto supermassive black holes (SMBHs) in their centres (Lynden-Bell 1969). As X-ray emission is ubiquitous in AGN, the *XMM-Newton* and *Chandra* X-ray missions have probed with unprecedented accuracy the AGN demographics, and hence they have mapped in detail the accretion history in the Universe (e.g. Ueda et al. 2014; Aird et al. 2015b; Miyaji et al. 2015; Ranalli et al. 2016; Fotopoulou et al. 2016; Georgakakis et al. 2017; Pouliasis et al. 2024). The majority of AGN are obscured by large amounts of dust and gas. This obscuring screen is believed to have the form of a torus, although direct imaging at mid-IR and sub-millimetre wavelengths have revealed a more complicated structure (e.g. Hönig et al. 2012; García-Burillo et al. 2016).

Additional constraints on the demographics of the AGN population come from the diffuse X-ray radiation that permeates the whole Universe, the X-ray background (Giacconi et al. 1962). This radiation comes from the superposition of all discrete point sources in their vast majority AGN (Mushotzky et al. 2000). The energy density of the X-ray background peaks at around 30 keV (Frontera et al. 2007; Churazov et al. 2007; Revnivtsev et al. 2003). Based on population synthesis models that attempt to reproduce the shape of the X-ray background, and especially its 30 keV hump, authors have found that a significant fraction of the sources that constitute this radiation must be associated with Compton-thick sources (Comastri et al. 1995; Gilli et al. 2007; Treister et al. 2009; Akylas et al. 2012; Ananna et al. 2019). These heavily obscured sources present column densities in excess of ≈10^{24} cm^{-2}, and hence the obscuration is caused by Compton scattering on electrons rather than photoelectric absorption (e.g. Hickox et al. 2017). Nevertheless, the X-ray background synthesis models appear to produce divergent results regarding the number of Compton-thick sources. On the low end, the models of Akylas et al. (2012) and Treister et al. (2009) yielded Compton-thick fractions of less than 20%. On the other end, the models of Ananna et al. (2019) predict Compton-thick fractions of the order of 50%. Recently, Carroll et al. (2023) attempted to constrain the fraction of Compton-thick sources by forward modelling the column density distribution of mid-IR selected AGN up to a redshift of $z = 0.8$. They estimate a Compton-thick fraction of 55% (but see Georgakakis et al. 2020).

A number of works have attempted to detect directly these highly obscured sources using the superb sensitivity of the *XMM-Newton* and *Chandra* missions (Georgantopoulos et al. 2009, 2013; Lanzuisi et al. 2015, 2017; Brightman et al. 2014; Koulouridis et al. 2016; Buchner et al. 2014; Georgakakis et al. 2017; Corral et al. 2019; Laloux et al. 2023). The identification of the Compton-thick sources is based on either the direct detection of the absorption turnover or the detection of a large equivalent width FeKα line, which is the smoking gun of heavy

* Corresponding author; ig@noa.gr

obscuration. However, as these missions operate in the relatively soft 0.5–10 keV band, they may miss a significant number of these heavily obscured sources.

The Burst Alert Telescope (BAT) instrument (Barthelmy et al. 2005) on board the *Neil Gehrels Swift* mission, (Gehrels et al. 2004), all-sky survey was very prolific in detecting a large number of candidate Compton-thick AGN due to its energy passband that extends to very hard energies, 14−195 keV. The 70-month BAT survey detected 728 non-blazar AGN. Ricci et al. (2015) identified 55 Compton-thick AGN among this sample up to a redshift of $z \sim 0.1$. Also using the 70-month BAT sample, Akylas et al. (2016) applied a Bayesian approach and identified a few tens of candidate Compton-thick AGN and assigned a column density probability distribution to each object. Both Ricci et al. (2015) and Akylas et al. (2016) found an observed Compton-thick fraction of less than 10% of the total AGN population. However, when Torres-Albà et al. (2021) used a volume-limited sample of Compton-thick AGN with *NuSTAR* spectra up to $z = 0.01$, they estimated an intrinsic Compton-thick fraction of about 20%. Their results refer to the column density range $N_H = 10^{24-25}$ cm^{-2}, the so-called transmission-dominated Compton-thick sources. This is the same column density range routinely probed by the Ricci et al. (2015) and Akylas et al. (2016) works. The work of Torres-Albà et al. (2021) suggests that a number of Compton-thick sources are so heavily obscured that their detection is arduous even in the BAT high energy band (see also Burlon et al. 2011). Some X-ray background synthesis models (e.g. Ananna et al. 2019) predict much higher Compton-thick fractions of up to 50%. This is because they assume an equally numerous fraction of Compton-thick AGN with extreme column densities in the range 10^{25-26} cm^{-2}, which have been dubbed reflection-dominated sources.

Based on their BAT sample, Akylas et al. (2016) derived the luminosity function of Compton-thick AGN. Ananna et al. (2022) derived the luminosity function using the Ricci et al. (2015) Compton-thick BAT sample, finding reasonable agreement with the work of Akylas et al. (2016). However, it soon became evident that the BAT's moderate sensitivity and spectral resolution may hamper the reliable identification of a number of faint sources as bona fide Compton-thick AGN. For this reason *NuSTAR* observations of the BAT-selected AGN have been systematically employed in order to accurately pinpoint the absorbing column density (e.g. Tanimoto et al. 2022; Torres-Albà et al. 2021; Marchesi et al. 2017, 2018; Georgantopoulos & Akylas 2019; Zhao et al. 2021; Silver et al. 2022).

2. Data

2.1. Neil Gehrels Swift

The *Swift* Gamma-Ray Burst (GRB) observatory (Gehrels et al. 2004) was launched in November 2004 and has been continually observing the hard X-ray (14−195 keV) sky with the BAT. The BAT is a large coded-mask telescope optimised to detect transient GRBs, and it was designed with a very wide field of view of $\sim 60 \times 100$ degrees.

The data presented in this paper stem from the analysis of the sources detected during the 70 months of observation by the BAT hard X-ray detector on the *Neil Gehrels Swift* GRB observatory (Baumgartner et al. 2013). The 70-month BAT survey is an almost uniform hard X-ray all-sky survey, with a sensitivity of 1.34×10^{-11} ergs s^{-1} cm^{-2} over 90% of the sky and 1.03×10^{-11} ergs s^{-1} cm^{-2} over 50% of the sky in the 14–195 keV band.

2.2. NuSTAR

The Nuclear Spectroscopic Telescope Array (*NuSTAR*, Harrison et al. 2013), launched in June 2012, is the first orbiting X-ray observatory that focuses light at high energies (E > 10 keV). It consists of two co-aligned focal plane modules (FPMs) that are identical in design. Each FPM covers the same 12 × 12 arcmin portion of the sky and comprises of four Cadmium-Zinc-Tellurium detectors. *NuSTAR* operates between 3 and 79 keV, and it provides an improvement of at least two orders of magnitude in sensitivity compared to previous hard X-ray observatories operating at energies E > 10 keV. This is because of its high spatial resolution 58 arcsec half-power diameter.

2.3. The Compton-thick active galactic nuclei in the BAT survey

In the 70-month BAT survey, 1171 hard X-ray sources have been detected down to 4.8σ and associated with 1210 counterparts. The majority of these sources are associated with AGN. In particular, there are 752 non-blazar AGN among these sources (Koss et al. 2022). Ricci et al. (2015) derived the X-ray spectra for the 70-month BAT survey sources, combining the *Neil Gehrels Swift* spectra with available *XMM-Newton*, *Chandra SUZAKU*, and *ASCA* data. The X-ray spectra showed that 55 sources are associated with Compton-thick obscuration. In another study, Akylas et al. (2016), again using the BAT 70-month survey, identify 42 sources with a probability above 30% of being Compton-thick. Although there is significant overlap between the two samples, there are a number of sources that have been characterised as Compton-thick in one sample but not in the other. Specifically, 35 sources are common between the two samples. Apart from the different methodology, it has to be noted that Akylas et al. (2016) uses only the *Neil Gehrels Swift* – that is, the BAT and the X-ray telescope (XRT) – data in their spectral analysis.

2.4. NuSTAR confirmation of BAT-selected Compton-thick active galactic nuclei

It was soon realised that the limited energy resolution of BAT may compromise the secure classification of Compton-thick AGN. In particular, it could be unclear whether a source was a bona fide Compton-thick AGN or just a heavily obscured source with a column density bordering the Compton-thick regime. Tanimoto et al. (2022) systematically analysed the *NuSTAR* observations of 52 candidate Compton-thick AGN in the sample of Ricci et al. (2017). They find that 28 objects are Compton-thick AGN at the 90% confidence interval. Their analysis was based on the XCLUMPY model of Tanimoto et al. (2019). The Clemson University group has performed another search for Compton-thick AGN in the BAT catalogues (e.g. Marchesi et al. 2017, 2018, 2019; Torres-Albà et al. 2021; Zhao et al. 2020, 2021; Silver et al. 2022; Sengupta et al. 2023). Their candidate Compton-thick AGN were originally selected either because their properties (either their Seyfert 2 optical type or the absence of a bright ROSAT counterpart) suggest the presence of substantial intrinsic absorption or because they lack soft 0.3–7 keV coverage. The authors primarily used the BORUS02 model of Baloković et al. (2019), but they also employed the MYTORUS model of Murphy & Yaqoob (2009). Despite the use of different models, the derived line-of-sight column densities agree reasonably well with Tanimoto et al. (2022), within the uncertainties. Georgantopoulos & Akylas

(2019) analysed the available *NuSTAR* observations of 19 sources from the Akylas et al. (2016) sample. The vast majority of these sources are common with the Ricci et al. (2015) sample. Georgantopoulos & Akylas (2019) used the absorption model of Murphy & Yaqoob (2009) together with a physically motivated thermal Comptonisation model (Titarchuk 1994) to represent the coronal emission. They find that all but two sources are associated with Compton-thick obscuration. Additional *NuSTAR* observations of the six Compton-thick candidates of Akylas et al. (2016) that are not common with Ricci et al. (2015) show that three sources are indeed Compton-thick: 2MASX J00253292+6821442, ESO426-G002, and NGC4941. The other three (NGC 3081, NGC 3588NED01, and ESO234-IG063) present lower obscuring column densities (Traina et al. 2021; Silver et al. 2022).

2.5. Models for Compton-thick absorption

In the following, we present a very concise overview of the models most often used to quantify the absorption and reflection in the *NuSTAR* observations of BAT-selected Compton-thick AGN. In Compton-thick objects, obscuration is primarily caused by scattering of X-ray photons on electrons and subsequent photoelectric absorption. There are a number of spectral codes available that utilise Monte Carlo simulations to model the absorption and reflection on the obscuring screen.

The MYTORUS Murphy & Yaqoob (2009) model assumes a tube-like azimuthally symmetric torus. The half-opening of the torus is assumed to be 60°, corresponding to a scenario where there are equal numbers of obscured and unobscured AGN. The model can decouple the line-of-sight and equatorial column densities. This is important for taking into account continuum variability and time delays between the direct (zeroth order or unscattered) continuum and the Compton-scattered continuum.

However, it has become apparent that the AGN torus is composed of many individual clouds. This is primarily because the 10 μm silicate feature appears as both an emission and absorption feature in Seyfert-2 galaxies, while the smooth torus models predict this feature only in absorption. In the infrared band, Nenkova et al. (2008) constructed spectral models for clumpy tori. They assumed a power law in the radial direction and a normal distribution in the elevation direction for the configuration of the clouds. Following this model, Tanimoto et al. (2019) constructed a new X-ray clumpy torus model designated as XCLUMPY by adopting the same geometry of clump distribution. The clumpy torus models predict a higher fraction of unabsorbed reflection components as observed in many obscured AGN. The line-of-sight column densities do not appear to differ significantly from the smooth tori model (see discussion in Torres-Albà et al. 2021).

One of the most widely used models is BORUS02 (Baloković et al. 2019). The reprocessing medium is assumed to be a sphere of uniform density with conical cutouts at both poles, approximating a torus with a variable covering factor. The half-opening angle of the polar cutouts, $\theta_{\rm tor}$, is measured from the symmetry axis towards the equator, and it ranges from zero (full covering) to 83°, corresponding to a disc-like 10% covering. The line-of-sight component, $N_H^{\rm los}$, can have a different column density than the column density of the torus ($N_H^{\rm tor}$) in order to account for clouds passing in front of the line of sight. In practice, this feature mimics the properties of a patchy torus.

Finally, Buchner et al. (2021) developed a clumpy torus named UXCLUMPY. Naturally, the patchy geometry results in strong Compton scattering, causing soft photons to escape also along Compton-thick sight lines. This model introduces an additional Compton-thick reflector near the corona, a necessary feature in order to achieve acceptable spectral fits to the *NuSTAR* spectra. This additional component can be interpreted as being part of the dust-free broad-line region, an inner wall or rim, or a warped disc.

3. The sample

3.1. Sample selection

We compiled our sample of Compton-thick AGN in the local Universe based on the *Neil Gehrels Swift* BAT 70-month survey. We started by using the Compton-thick AGN samples selected by Ricci et al. (2015) and Akylas et al. (2016). Finally, we complemented our sample with a few additional Compton-thick sources reported by the Clemson group (see Table A.1). The condition for inclusion of these sources in our sample is that they are detected in the 70-month survey, and thus they are included in the sample of Baumgartner et al. (2013). These sources evaded classification by both Ricci et al. (2015) and Akylas et al. (2016). As *NuSTAR* observations exist for all of these sources, there is an accurate determination of the column density available. We included all sources with column densities consistent with $N_H = 10^{24}$ cm^{-2} at the 90% confidence level. We note that the selected threshold value is somewhat below the column density that corresponds to $\tau = 1$ for Compton scattering. We included only sources with redshift $z < 0.05$, corresponding roughly to 200 Mpc. Our sample contains 45 sources and is presented in Table A.1. The first reference in column (8) of Table A.1 denotes the origin of the column density. Nearly all of our sources have a column density much lower than 10^{25} cm^{-2}, with the exception being NGC 1068, which has a borderline column density of $N_H = 10^{+100}_{-0.80} \times 10^{25}$ cm^{-2}. We chose to exclude this source and restrict our analysis only to the 10^{24}–10^{25} cm^{-2} sources. This is because most current models for Compton-thick absorption do not produce reliable results at such extreme column densities.

The majority of the column densities comes from the work of either Zhao et al. (2021), Marchesi et al. (2018), or Tanimoto et al. (2022). For a vast majority of the sources, the differences between the column densities are consistent within the uncertainties. An exception is ESO 005-G004, where Tanimoto et al. (2022) using XCLUMPY find that the source is heavily obscured, while Marchesi et al. (2018), using MYTORUS, find that the source is marginally Compton-thick. Zhao et al. (2021), using BORUS02, find a column density of $N_H \approx 5 \times 10^{24}$ cm^{-2}. The differences are probably attributable to the fact that the different models prefer a significantly different value for the photon-index that counteracts the derived column density. Finally, we note that the luminosities are estimated in a consistent manner, as described in the section below.

3.2. Estimation of absorption-corrected luminosities

The selected sample of local Compton-thick AGN has been studied with a variety of spectral models in the literature. While estimations of the line-of-sight column density, N_H, are reasonably robust and model independent (e.g. Saha et al. 2022) if X-ray data above 10 keV are included, the remaining parameters can be quite uncertain. This can cause significant discrepancies, particularly when estimating the absorption-corrected luminosity. For consistency, we assumed a single X-ray spectral model for all the sources. Given this model, the observed BAT flux, and

the N_H estimates from the literature, we calculated the corresponding intrinsic luminosity for each AGN in our sample. We used the spectral model assumed by Ananna et al. (2022) in their study of the X-ray luminosity function of *NuSTAR* sources. It is a modification of the model assumed by Ueda et al. (2014) where the torus absorption and reflection are instead modelled using BORUS02. For Compton-thick sources, a photon index of $\Gamma = 1.8$ was used with an energy cut-off of 200 keV, an inclination angle of 72 deg, and a half-opening angle of 60 deg. To check the validity of our derived luminosities, we also used the XCLUMPY model. We found no significant differences in our derived luminosities.

For a rigorous treatment of the N_H and flux uncertainties, for each source we generated 2000 random samples of N_H flux pairs and calculated the corresponding luminosity. The sampling was done assuming a generalised extreme distribution parameterised in such a way that its median corresponds to the quoted value of the N_H, flux in Table A.1 and the fifth and 95th percentiles correspond to the respective error interval. This distribution is recommended to reproduce strong asymmetric confidence intervals Possolo et al. (2019).

3.3. Detection probability and selection biases

The sensitivity curve (flux limit versus area covered) of the BAT survey is not uniform across the sky (Baumgartner et al. 2013). Towards the flux limit's bright end (low sensitivity), the area covered is the largest, but a considerable number of sources are less likely to be detected. This is because they will present a faint flux due to having a low luminosity or a higher column density or simply because they are found at a higher redshift. This introduces some biases that have to be addressed and quantified in order to accurately estimate the X-ray luminosity function of the intrinsic population of the Compton-thick sources. We then needed to estimate the probability that a Compton-thick source with a column density N_H, redshift z, and intrinsic luminosity L_X will be detected in the BAT survey. To this end, we used the BORUS02 model as above to build the sensitivity maps. We assumed a photon index of $\Gamma = 1.8$, an inclination angle $i = 72$ deg, and a torus half-opening angle $\sigma = 60$ deg. Then we calculated the expected flux at a given set of z, L_X, and N_H using a grid of 50 bins in each parameter. The probability of detecting a source was derived by convolving the expected flux with the area curve of BAT (Baumgartner et al. 2013). The upper and lower panels of Fig. 1 present the detection probability maps as a function of redshift and intrinsic X-ray luminosity for a source with $N_H \sim 10^{24}$ cm^{-2} and $N_H \sim 10^{25}$ cm^{-2}, respectively.

3.4. Column density, redshift, and luminosity distributions

The redshift distribution of our sample is given in Fig. 2. The redshift distribution peaks at $z \approx 0.015$. In the same figure we present the distribution of the unabsorbed luminosity in the 10–50 keV band as well as the hydrogen column density, N_H, distribution. The column density distribution is dominated by sources just above the threshold of $N_H = 10^{24}\,cm^{-2}$, while there is a significant deficit of sources with $\log(N_H)[\mathrm{cm}^{-2}] > 24.5$. This can most probably be attributed to a selection effect. The widest possible range of column densities can be detected only at the lowest redshifts, owing to the limited sensitivity of the BAT survey. This is evident in Fig. 3, where we plot the N_H values versus the redshift of each source. It is apparent that there is a strong correlation between N_H and redshift in the sense that at the highest redshifts, we can detect only Compton-thick AGN with relatively low column densities. In the previous section, we presented the detection probability as a function of intrinsic X-ray luminosity and redshift for a given column density. From Fig. 1, we observed that sources such as NGC1068 with an intrinsic luminosity $L_X \approx 10^{44}$ erg s^{-1} and column density $N_H \sim 10^{25}$ cm^{-2} can be detected (detection probability $P_{detection} > 0.5$) up to a redshift of $z = 0.03$. A heavily obscured Compton-thick source with $N_H = 10^{25}$ cm^{-2} must have an intrinsic luminosity of $L_X > 3 \times 10^{44}$ erg s^{-1} in order to be detected at the redshift limit of our survey $z = 0.05$.

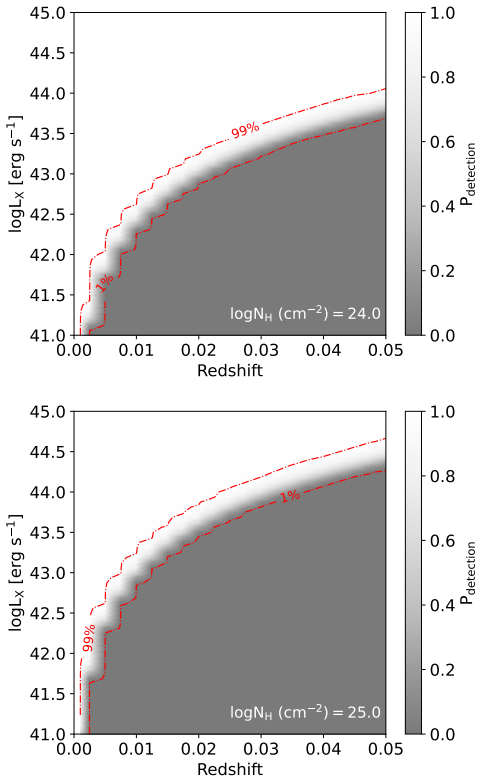

Fig. 1. Detection probability maps as a function of the intrinsic X-ray luminosity and redshift for a source with an intrinsic column density of $N_H \sim 10^{24}$ cm^{-2} (upper) and $N_H \sim 10^{25}$ cm^{-2} (lower). The red lines indicate the probability of detection at 1% and 99%.

4. Analysis

4.1. X-ray luminosity function

We defined the differential X-ray luminosity function, ϕ, as the number of sources N per co-moving volume V and per logarithmic interval $\log L_X$ as a function of redshift, z, and luminosity, L_X,

$$\phi(L_X, z) = \mathrm{d}\Phi(L_X, z)\mathrm{d}\log L_X = \frac{d^2N(L_X, z)}{\mathrm{d}V\mathrm{d}\log L_X}. \quad (1)$$

Following Akylas et al. (2016) and Ananna et al. (2022), we modelled the differential luminosity function with a broken power law (Maccacaro et al. 1984; Barger et al. 2005), defined as

$$\mathrm{d}\Phi(L_X)\mathrm{d}\log L_X = A \times \left[\left(\frac{L_X}{L_*}\right)^{\gamma_1} + \left(\frac{L_X}{L_*}\right)^{\gamma_2}\right]^{-1}, \quad (2)$$

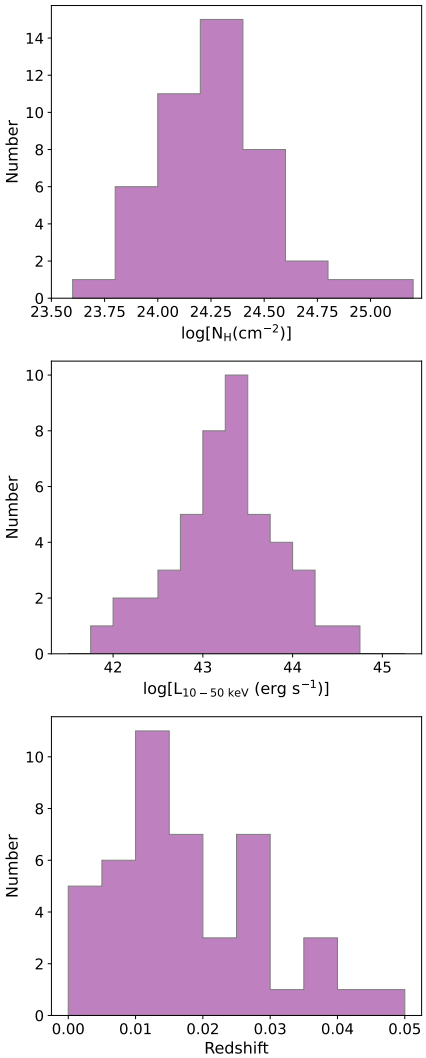

Fig. 2. Distributions of the hydrogen column density (top panel), the 10−50 keV absorption-corrected luminosity (middle panel), and redshift (bottom panel) for our sample.

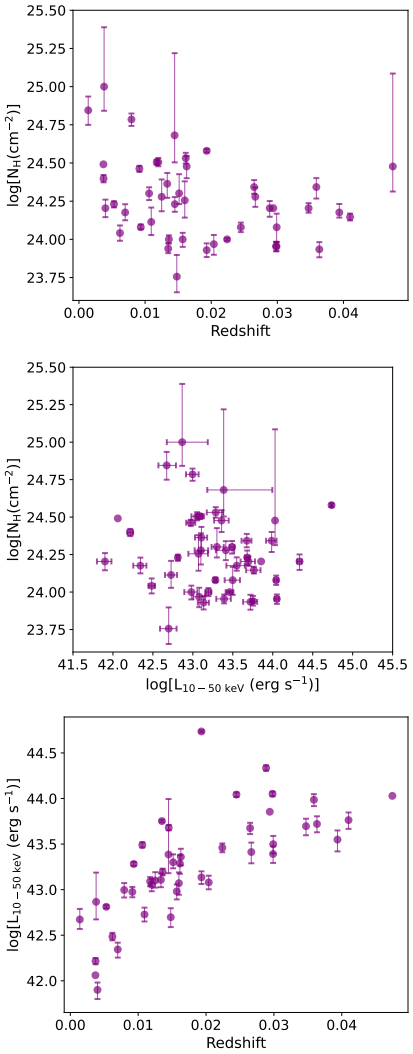

Fig. 3. Column density versus redshift (top panel); column density versus X-ray absorption-corrected luminosity (middle panel); X-ray absorption-corrected luminosity versus redshift (bottom panel).

where A is a normalisation factor and L_* is the break luminosity, while γ_1 and γ_2 are the slopes of the power law at the faint-end and the bright-end slopes, respectively.

Furthermore, we calculated the binned luminosity function for visualisation purposes following the Page & Carrera (2000) method that is based on the $1/V_{\rm max}$ method (Schmidt 1968; Avni & Bahcall 1980). After dividing the sample of Compton-thick sources into redshift, luminosity, and hydrogen column density bins, the binned luminosity function could be estimated as

$$\phi(L_X, z, N_H) = \frac{\langle N \rangle}{\iiint \Omega(L_X, z, N_H) \mathrm{d}V \mathrm{d}z \, \mathrm{d}\log L_X \, \mathrm{d}\log N_H \, \mathrm{d}z}, \quad (3)$$

where $\langle N \rangle$ is the number of sources in each bin, $\mathrm{d}V\mathrm{d}z$ is the differential co-moving volume, and Ω represents the survey area (Sect. 3.3).

4.2. Fit and parameter estimation

We used Bayesian inference to estimate the parametric form of the X-ray luminosity function following the approach of Loredo (2004). The full description of the method is given in Pouliasis et al. (2024). Here, we just outline the basic concepts. Given a data set of n observations, $D = \{d_i; i = 1, \ldots, n\}$, and a model for the X-ray luminosity function defined by a set of parameters $\mathbf{\Theta}$, according to Bayes' theorem, the posterior probability (i.e. the probability of obtaining the selected model given the observational data) is

$$P(\mathbf{\Theta}|D) = \frac{P(D|\mathbf{\Theta})P(\mathbf{\Theta})}{P(D)}. \quad (4)$$

The likelihood, $\mathcal{L} = P(D|\mathbf{\Theta})$, is the probability of obtaining the observational data given the model. The prior, $P(\mathbf{\Theta})$, is the a priori probability for the parameters of the model. The term $P(D)$ is the evidence of the model: $P(D) = \int P(\mathbf{\Theta}|D) d\mathbf{\Theta}$. We derived the posterior probability distribution of the model parameters using the nested sampling Monte Carlo algorithm MLFriends (Buchner & Bauer 2017), implemented in the `UltraNest` package. Nested sampling algorithms allow for the tracing of the posterior distribution of the model, given a data set, while at the same time calculating the Bayesian evidence. The Bayesian approach allows for a rigorous treatment of the uncertainties in the X-ray properties of the sources. During the inference process, we assumed flat priors for the model parameters, either

Table 1. Best-fit values and 2σ errors for the parameters of the luminosity function.

Parameter	Prior	Best value
$\log A$ (Mpc^{-3})	–7, –3	$-4.40^{+0.40}_{-0.50}$
$\log L_*$ (erg s^{-1})	42, 46	$42.86^{+0.44}_{-0.43}$
γ_1	–2, 2	$0.01^{+0.51}_{-0.74}$
γ_2	1, 6	$1.72^{+0.40}_{-0.37}$

Table 2. Compton-thick AGN fractions.

Sample	Fraction	Redshift
This work (×)	$0.24^{+0.05}_{-0.05}$	<0.05
Burlon et al. (2011) (×)	$0.20^{+0.09}_{-0.06}$	<0.1
Ricci et al. (2017) (×)	$0.27^{+0.04}_{-0.04}$	<0.1
Torres-Albà et al. (2021) (×)	$0.20^{+0.05}_{-0.05}$	<0.01
Ueda et al. (2014) (×)	$0.27^{+0.05}_{-0.05}$	<0.1
Buchner et al. (2015) (†)	$0.43^{+0.10}_{-0.10}$	≈0
Laloux et al. (2023) (†),(1)	$0.21^{+0.16}_{-0.10}$	<0.5
Akylas et al. (2024) (2)	$0.25^{+0.05}_{-0.05}$	z<0.02
Boorman et al. (2024) (3)	$0.35^{+0.06}_{-0.06}$	<0.044
Ananna et al. (2019) (4)	$0.33^{+0.10}_{-0.10}$	<0.1

Notes. Column Description: (1) Sample. (2) Compton-thick fraction ($N_H = 10^{24-25}$ cm^{-2}). (3) Redshift. The × denotes fractions are based on BAT in the local Universe. (†)symbol denotes fractions based on *XMM-Newton* and *Chandra* observations at higher redshifts. (1)Estimate based on mid-IR priors. (2)AGN sample selected using *WISE* warm colours. (3)AGN sample selected using warm *IRAS* colours. (4)Based on X-ray background synthesis models.

uniform or log-uniform, that span a reasonably broad range of the parameter space according to previous studies in the literature (Akylas et al. 2016; Ananna et al. 2022). The range of our priors is consistent with the $1/V_{\rm max}$ non-parametric luminosity function. In Table 1, we provide the minimum and maximum values allowed in the flat priors we used for the parameters of our X-ray luminosity function model.

The log-likelihood of this process can be written as

$$\ln \mathcal{L}(\{d_i\}|\mathbf{\Theta}) = -\lambda + \sum_i \ln \iiint P_i(L_{\rm X}, z, N_{\rm H}|\mathbf{\Theta})\, {\rm d}V {\rm d}z {\rm d}\log N_{\rm H}\, {\rm d}\log L_{\rm X}\, {\rm d}z. \quad (5)$$

The parameter λ is the expected number of observed sources for a Poisson process, given an X-ray luminosity function model with parameters $\mathbf{\Theta}$:

$$\lambda = \iiint \phi(L_{\rm X}, z, N_{\rm H}|\mathbf{\Theta})\Omega(L_{\rm X}, z, N_{\rm H})\, {\rm d}V {\rm d}z {\rm d}\log N_{\rm H}\, {\rm d}\log L_{\rm X}\, dz, \quad (6)$$

where Ω is the survey sensitivity function and ϕ is the luminosity function. The parameter P_i in Eq. 5 is given by

$$P_i(L_{\rm X}, z, N_{\rm H}|\mathbf{\Theta}) = p(d_i|L_{\rm X}, z, N_{\rm H})\, \phi(L_{\rm X}, z, N_{\rm H}|\mathbf{\Theta})\, \Omega(L_{\rm X}, z, N_{\rm H}), \quad (7)$$

where $p(d_i|L_{\rm X}, z, N_{\rm H})$ is the probability of the source i being at redshift z with column density N_H and luminosity L_X. This probability is given by the posterior probability distributions we obtained during the X-ray spectral analysis. We have included in this term the sensitivity function of the survey Ω. The integral involving P_i can be calculated using an importance sampling Monte Carlo integration technique (Press et al. 1992). The integration limits used in Eq. (5) are [0,0.05], [41.0,46.0], and [23.5,26.0] for the parameters z, $\log L_X$, and $\log N_H$, respectively.

5. Results

5.1. The 10–50 keV X-ray luminosity function

Here we present the best-fit results and the confidence intervals for the parameters of the luminosity function (Eq. (2)). These parameters are the normalisation, A; the break, L_*; and the faint-, γ_1, and bright-end, γ_2, slopes. The values together with the 68% confidence intervals are given in Table 1. In Fig. 4, we present the corner plots. The relationships between the various parameters are depicted through scatter plots of all possible sets of parameters (e.g. $L_\star$ versus γ_1). The diagonal boxes illustrate the marginalised posterior distribution of each parameter. The break luminosity is $\log L_\star$[erg s^{-1}] ≈ 43, while the faint-end of the luminosity function is quite flat, having a slope of $\gamma_1 = 0.01^{+0.51}_{-0.74}$. This suggests that there may not be ample room for a faint population of Compton-thick AGN.

In Fig. 5, we present the X-ray luminosity function in the 10–50 keV band. In the left panel, we compare the parametric luminosity function with the non-parametric one derived using the $1/V_{\rm max}$ method. In the right panel of Fig. 5, we compare our luminosity function with those of Akylas et al. (2016) and Ananna et al. (2022). These luminosity functions have been derived in the 20–40 keV and 14–195 keV band, respectively. We homogenised the different luminosity functions to the 10–50 keV band using the corresponding spectral models assumed by each work.

The luminosity function of Ananna et al. (2022) lies somewhat above our estimate, especially around $L_\star$. It has to be noted that the two luminosity functions contain different sets of objects despite the fact that they both come from the 70-month BAT survey. Moreover, it has to be taken into account that the luminosity function of Akylas et al. (2016) is not corrected for obscuration. In Fig. 5 (right panel), we also compare our luminosity function with the X-ray background synthesis models of Ananna et al. (2022). These refer to both the Compton-thick population with column densities $N_H = 10^{24-25}$ cm^{-2} and $N_H = 10^{25-26}$ cm^{-2}, respectively. We can compare our luminosity function only with the former, as they refer to the same column density range. It appears the model predicts a very high number of Compton-thick AGN at low luminosities, a few times 10^{42} erg s^{-1}. This is rather at odds with our findings and even with the luminosity function of Ananna et al. (2022).

5.2. Comparison with the 2–10 keV luminosity function

Next, we compare our luminosity function with other Compton-thick luminosity functions derived in the softer 2–10 keV band. Ueda et al. (2014) constructed the luminosity function in the 2–10 keV band by compiling data from various missions operating in these wavelengths. They also used the BAT nine-month survey, which contains a number of known Compton-thick AGN, to determine their fraction in the local Universe. Their luminosity function has been used to model the spectrum of the X-ray background in the energy range 1–1000 keV, resulting in very good agreement with the data. In Fig. 6,

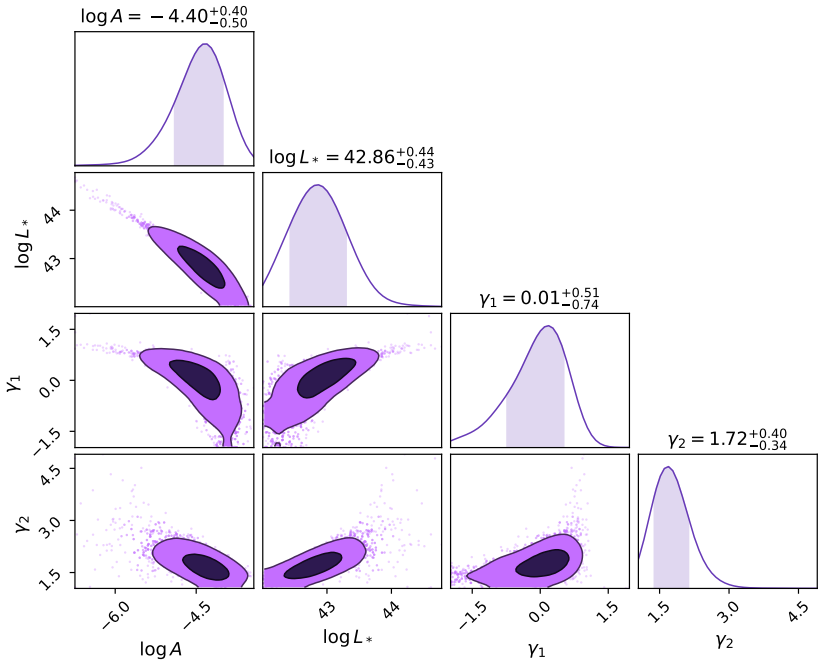

Fig. 4. One-dimensional (diagonal panels) and two-dimensional marginalised posterior distributions for the double power-law model parameters. The shaded areas in the 2D posterior distributions correspond to 1σ and 2σ confidence levels (2D values; i.e. 39% and 86% respectively). The shaded areas for the 1D posteriors correspond to the 1σ confidence level.

we compare the Ueda et al. (2014) with our luminosity function in the 2–10 keV band. We plot the luminosity function of Ueda et al. (2014) that refers to the 10^{24-25} cm^{-2} column density range. For the conversion of our luminosity function in the 2–10 keV band, we used the same spectral model used in Sections 3.2 and 3.3. Their luminosity function is in good agreement with ours at luminosities brighter than $L_X \approx 10^{42}$ erg s^{-1}. However, the former appears to present an upturn at faint luminosities.

In Fig. 6 we also plot the luminosity function derived by Buchner et al. (2015) as a fish-shaped diagram. This region gives the 10%–90% quantiles as a range for the uncertainty of the luminosity function. We note that the luminosity function of Buchner et al. (2015) typically refers to the $N_H = 10^{24-26}$ cm^{-2} column density range. However, the reflection-dominated sources with $N_H = 10^{25-26}$ cm^{-2} are very sparsely sampled because of the extreme obscuration (e.g. Buchner et al. 2015). It is therefore reasonable to assume that the luminosity functions of Buchner et al. (2015) quoted in the $N_H = 10^{24-26}$ cm^{-2} column range provide very good approximations of the luminosity function in the $N_H = 10^{24-25}$ cm^{-2} column density range. Finally, we plot the luminosity function derived by Aird et al. (2015b) for the $N_H = 10^{24-25}$ cm^{-2} column density range.

5.3. The observed fraction of Compton-thick active galactic nuclei

We estimated the observed cumulative fraction of Compton-thick AGN in different redshift bins. For a given redshift, z_i, this is defined as the ratio of the Compton-thick AGN up to z_i over the total number of (non-blazar) AGN in the same redshift bin. The fraction is given in Fig. 7. The fraction is the highest in the first redshift bin $z < 0.01$, with $f \approx 0.17 \pm 0.06$. According to Fig. 1, an obscured source with $N_H \approx 10^{24}$ cm^{-2} and $L_X < 3 \times 10^{42}$ erg s^{-1} cannot be easily detected even in our first redshift bin, that is, up to z = 0.01 (≈43 Mpc). This is exacerbated at higher column densities. An AGN that is obscured by a column density of 10^{25} cm^{-2} can be detected at z = 0.01 only if it has a luminosity above $L_X > 10^{43}$ erg s^{-1}. This means that our estimated fraction $f = 0.17$ can only be considered as a lower limit to the fraction of Compton-thick AGN.

5.4. The intrinsic fraction of Compton-thick active galactic nuclei based on the luminosity function

Our obscuration-corrected luminosity function provides us with the opportunity to estimate the intrinsic fraction of Compton-thick AGN. Towards this end, we estimated the intrinsic number of Compton-thick AGN in the 2–10 keV band using the following expression:

$$\int_{z=0}^{z=0.05} \int_{\log L_X=42}^{\log L_X=45} \Phi(L)\, dV dz\, d\log L_X\, dz. \quad (8)$$

Our luminosity function predicts 112 Compton-thick AGN with a luminosity of $L_X > 10^{42}$ erg s^{-1} (10–50 keV) over the whole sky up to a redshift of $z = 0.05$. Then we compared with the number of Compton-thin AGN ($N_H = 10^{20-24}$ cm^{-2}) derived using the above expression and the Ueda et al. (2014) Compton-thin luminosity function. The number of Compton-thin AGN is 359. The fraction of Compton-thick sources is defined as

$$f_{24-25} = N_{24-25}/(N_{20-24} + N_{24-25}), \quad (9)$$

where N_{24-25} and N_{20-24} are the number densities of objects in the column density range $N_H = 10^{24-25}$ cm^{-2} and $N_H = 10^{20-24}$ cm^{-2}; The above number densities are derived from this current work and Ueda et al. (2014), respectively. The fraction of Compton-thick AGN versus the total number of AGN is 24 ± 5%. The error is derived by sampling the uncertainty space of our Compton-thick luminosity function parameters at the 68% confidence level.

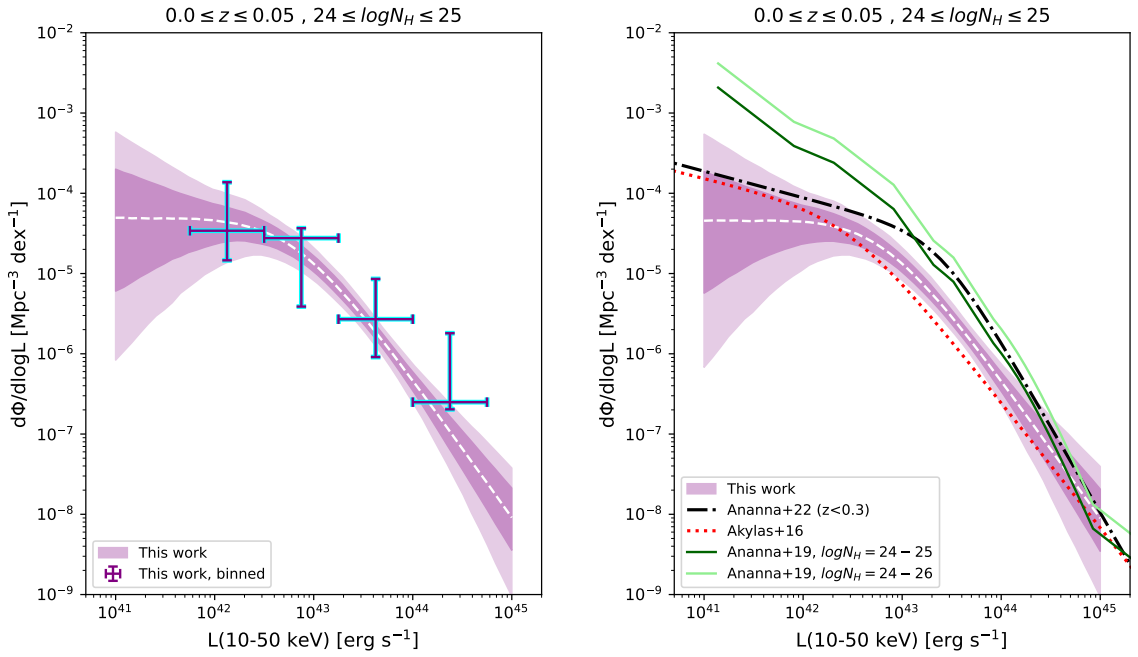

Fig. 5. The X-ray luminosity function in the 10–50 keV band. Left panel: Compton-thick ($\log N_H[cm^{-2}] = 24 - 25$) X-ray luminosity function in the redshift range $0.0 \leq z \leq 0.05$. The shaded regions represent the 68% and 95% confidence intervals. The points show the binned $1/V_{max}$ luminosity function with the corresponding 68% uncertainties. Right panel: Our luminosity function compared with those of (Akylas et al. 2016; Ananna et al. 2022) and also by the population synthesis models of Ananna et al. (2019). The best-fitting model of the latter is evaluated at the mean redshift of our analysis ($z = 0.025$).

Next, we compare our findings with the Compton-thick fractions derived in the literature. Ricci et al. (2015) derived a fraction of 27 ± 4% by modelling the absorption distribution of the $N_H = 10^{24-25}$ cm^{-2} Compton-thick AGN from the BAT 70-month survey. This figure is entirely compatible with our estimates. Ueda et al. (2014) derived the absorption function in the local Universe using data from the BAT nine-month survey. They found similar fractions for Compton-thick AGN in the same column density range ($N_H = 10^{24-25}$ cm^{-2}). In general, it appears that a consensus has been reached at least regarding the number of Compton-thick AGN with $N_H = 10^{24-25}$ cm^{-2} in the local Universe (see also Burlon et al. 2011; Georgantopoulos & Akylas 2019; Torres-Albà et al. 2021). All the above results have been derived on the basis of BAT detections. This is not surprising since the large pass-bands of the *Neil Gehrels Swift* mission facilitates the detection of Compton-thick AGN.

Recently, Boorman et al. (2024) constrained the Compton-thick fraction in the local Universe ($z < 0.044$) using a sample of 122 AGN primarily selected to have warm *IRAS* colours. By fitting the available X-ray spectra, they estimated a Compton-thick fraction of 35 ± 6%. In a similar work, Akylas et al. (2024) used a sample of *WISE*-selected AGN up to redshifts of $z = 0.02$. The estimated Compton-thick fraction is 0.25 ± 0.05 %.

Beyond the local Universe, the results based primarily on the modelling of *Chandra* and *XMM-Newton* spectra present considerable scatter. A summary of the estimated fraction of Compton-thick AGN in the $N_H = 10^{24-25}$ cm^{-2} column density range is given in Table 2. We note that some of these works (Buchner et al. 2015; Laloux et al. 2023) quote the fraction of Compton-thick AGN in the column density range $N_H = 10^{24-26}$ cm^{-2} despite the fact that the number of detected sources with $>10^{25}$ cm^{-2} is extremely small (see discussion in Buchner et al. 2015). For this reason, it can be safely assumed that the observed fraction of Compton-thick AGN in the $N_H = 10^{24-25}$ cm^{-2} column density range is approximately equal to the fraction of Compton-thick sources in the $N_H = 10^{24-26}$ cm^{-2} range.

It is unclear whether the fraction of Compton-thick AGN increases with redshift. Buchner et al. (2015) find that the fraction is consistent with being constant, while Lanzuisi et al. (2017) find a steep increase at high redshifts. If indeed the fraction increases with redshift, this may mark a genuine evolution of the obscuring medium in Compton-thick AGN with cosmic time. For example, it has been proposed that the excess obscuration at higher redshifts is associated with the host galaxy of the AGN (e.g. Gilli et al. 2022). Alternatively, the excess number of Compton-thick AGN could be an artefact of the moderate photon statistics at higher redshifts combined with the limited pass-band of the *Chandra* and *XMM-Newton* missions. Interestingly, Laloux et al. (2023) analysed the X-ray spectra of AGN in the COSMOS field using a novel method. They derived the 6 μm luminosity of the AGN component to use it as a prior for the determination of the X-ray obscuration. At redshifts of $z < 0.5$, their method yields results that are compatible with the BAT results in the local Universe. At higher redshifts, Laloux et al. (2023) could only derive upper limits for the Compton-thick fraction.

5.5. NuSTAR number counts constraints

In this section, we explore the possible constraints that can be posed by the serendipitously selected *NuSTAR* Compton-thick AGN. Lansbury et al. (2017b) present the sources that have been detected in the 40-month serendipitous source catalogue covering 13 deg^2. Making use of this catalogue, Lansbury et al. (2017a) selected the candidate Compton-thick AGN by applying a hardness ratio criterion (i.e. a hard-to-soft band ratio BR_{Nu} >

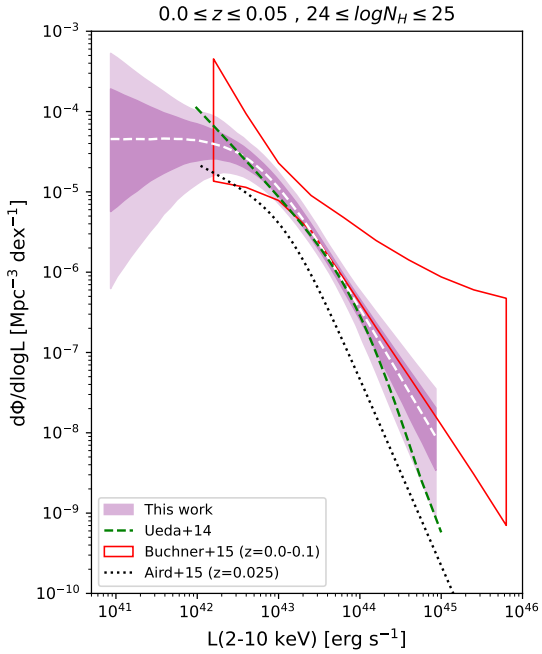

Fig. 6. X-ray luminosity function ($\log N_H[cm^{-2}] = 24 - 25$) in the 2–10 keV band. The shaded regions represent the 68% and 95% confidence intervals. The green dash line corresponds to the Compton-thick luminosity function of Ueda et al. (2014). The dotted line denotes the luminosity function of Aird et al. (2015a). Finally, the red fish-shaped diagram corresponds to the luminosity function of Buchner et al. (2014) (see text for details).

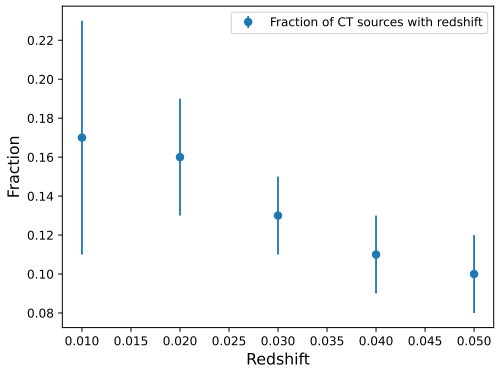

Fig. 7. Observed fraction of Compton-thick AGN as a function of redshift.

1.7) and using the 3–8 keV and 8–24 keV bands. This hardness ratio was chosen based on the spectrum of a Compton-thick AGN when assuming the model of Baloković et al. (2014). They found four candidate sources at small redshifts within $z < 0.07$. Subsequent *NuSTAR* spectral analysis (Lansbury et al. 2017a) appears to be consistent with Compton-thick absorption. Recently, Greenwell et al. (2024) presented the new serendipitous *NuSTAR* catalogue covering 40 deg^2. They found three additional Compton-thick AGN by applying the same hardness ratio criterion, $BR_{Nu} > 1.7$, within the same redshift range. Out of these seven sources, only four are within the range of our derived luminosity function. We used these candidate Compton-thick sources to derive the number count distribution in the 8–24 keV band in order to compare it with our Compton-thick luminosity function. In Fig. 8 (left), we compare the *NuSTAR* and BAT number counts within $z = 0.05$ with the predictions of our luminosity function. In the same figure (right), we compare the *NuSTAR* number counts within $z = 0.07$ with the predictions of our luminosity function extrapolated to $z = 0.07$ in order to exploit the better number statistics. We assigned weights for each source in the *NuSTAR* number counts. For sources with X-ray spectral fits in Lansbury et al. (2017a), the weight was calculated taking the full N_H distribution into account. For the remaining sources, we used the error on the BR_{Nu} hardness ratio as the weight. The errors on the BAT and *NuSTAR* number counts were estimated following Mateos et al. (2008).

In the same plot we give the predictions of the Ananna et al. (2019) X-ray background synthesis model. It appears that our luminosity function lies well below the *NuSTAR* number counts in the $z < 0.07$ redshift range. The luminosity function of Ananna et al. (2019) derived from their X-ray background synthesis model, which includes the constraints of the *NuSTAR* Compton-thick number counts, is actually much closer. Their model includes a number of reflection-dominated Compton-thick $N_H = 10^{25-26}$ cm^{-2} AGN equal to the number of the transmission-dominated Compton-thick AGN. Taken at face value, this result could imply that the vast majority of the Compton-thick population are associated with reflection-dominated AGN that remain undetected by BAT due to its limited sensitivity. However, caution has to be exercised in the interpretation of the *NuSTAR* number counts. Akylas & Georgantopoulos (2019) demonstrated that the *NuSTAR* number counts of the full X-ray source population in the 8–24 keV and the 3–8 keV bands are incompatible with the BAT and *Chandra* number counts, respectively. In particular, there is an upturn in the 8–24 keV *NuSTAR* number counts at fluxes of a few 10^{-14} erg cm^{-2} s^{-1}. This could be attributed to a very strong Eddington bias at these faint fluxes Civano et al. (2015).

5.6. Possibility of a missing population of Compton-thick active galactic nuclei

Additional constraints on the number of Compton-thick AGN can be provided by the X-ray background synthesis models. As we have explained in the previous section, many of these models assume the existence of large numbers of extremely obscured Compton-thick sources with $N_H > 10^{25}$ cm^{-2}. However, given the uncertainties of the X-ray background spectrum at high energies, around 30 keV, it is by no means certain that the addition of these reflection-dominated sources is required to fit the background (e.g. Akylas et al. 2012). Actually, Comastri et al. (2015) have argued that a large number of heavily buried Compton-thick AGN could be present without violating the X-ray and IR background constraints. NGC 4418 is usually considered the prototype for this population (e.g. Sakamoto et al. 2010). One way to compile large samples of these extreme sources would be to study in X-rays the volume-limited samples of nearby AGN detected in either the optical or the IR bands. Akylas & Georgantopoulos (2009) examined the *XMM-Newton* spectra of the Seyfert-2 galaxies in the Ho et al. (1997) sample of nearby galaxies. They found a Compton-thick AGN fraction compatible with the findings in this work. More recently, Asmus et al. (2020) compiled the most comprehensive sample of candidate AGN in the nearby Universe, z<100 Mpc. Detailed studies of these sources with *NuSTAR* have provided a significant advance in the study of the less luminous local Compton-thick AGN (Akylas et al. 2024).

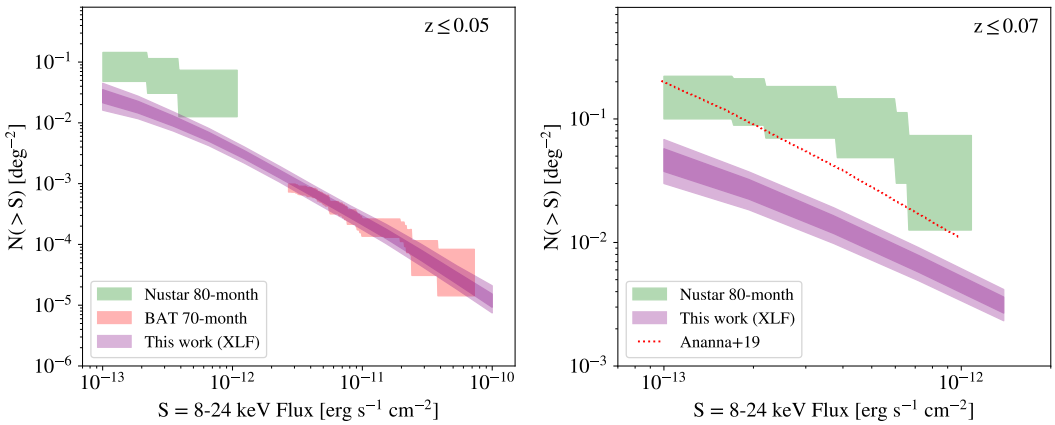

Fig. 8. Observed and predicted number counts in the 8–24 keV band. (a) Left: Redshift range $z < 0.05$. The BAT 70-month survey number counts are plotted (red shaded diagram) together with the predictions of our luminosity function (shaded curve). The *NuSTAR* number counts are shown with the green diagram. (b) Right: Redshift range $z < 0.07$. The green shaded diagram corresponds to the *NuSTAR* number counts. The predictions of our luminosity function are depicted with the shaded curve. The red dotted line denotes the predictions of the X-ray background synthesis model of Ananna et al. (2019) in the $10^{24} - 10^{26}$ cm^{-2} column density range.

6. Summary

We have compiled a new sample of bona fide Compton-thick AGN based on the initial selection of candidates from the 70-month BAT survey. Then, we confirmed that these are Compton-thick sources using the column densities derived by *NuSTAR* spectral analysis. Our final sample consists of 44 sources up to a redshift of $z = 0.05$ with intrinsic luminosities as faint as $L_X \approx 3 \times 10^{41}$ erg s^{-1} in the 10–50 keV band. All of these sources have column densities in the range $N_H = 10^{24-25}$ cm^{-2}. Our primary goal in this work is to derive a robust X-ray luminosity function for Compton-thick AGN in the local Universe and, based on this, to securely estimate the fraction of Compton-thick AGN. The derivation of the luminosity function follows a Bayesian methodology where the errors on the column densities and the luminosities are fully taken into account. Our results can be summarised as follows:

- The luminosity function is described with a double power law where the faint- and bright-end slopes are $\gamma_1 = 0.01^{+0.51}_{-0.74}$ and $\gamma_2 = 1.72^{+0.40}_{-0.37}$, respectively. The break of the luminosity function is $\log L_*[\text{erg s}^{-1}] = 42.9^{+0.44}_{-0.43}$. The flat slope of the faint end of the luminosity function rather argues against a numerous population of faint Compton-thick AGN.
- The fraction of Compton-thick AGN relative to the total AGN population is 24 ± 5%. This was estimated using our Compton-thick luminosity function and the Compton-thin luminosity function of Ueda et al. (2014).

In conclusion, there appears to be a consensus on the number of Compton-thick AGN in the local Universe, at least when these are derived from the BAT data. At higher redshifts, a significant scatter is observed in the estimated fraction of Compton-thick AGN. If a higher fraction is indeed confirmed by future studies, such as those that will be performed with the *ATHENA* mission, this would suggest a strong evolution of the AGN Compton-thick population with cosmic time.

Acknowledgements. We thank the anonymous referee for very constructive comments. We acknowledge financial support by the European Union's Horizon 2020 programme "XMM2ATHENA" under grant agreement No 101004168. The research leading to these results has also received funding from the European Union's Horizon 2020 Programme under the AHEAD2020 project (grant agreement n. 871158).

References

Aird, J., Alexander, D. M., Ballantyne, D. R., et al. 2015a, ApJ, 815, 66
Aird, J., Coil, A. L., Georgakakis, A., et al. 2015b, MNRAS, 451, 1892
Akylas, A., & Georgantopoulos, I. 2009, A&A, 500, 999
Akylas, A., & Georgantopoulos, I. 2019, A&A, 625, A131
Akylas, A., Georgakakis, A., Georgantopoulos, I., Brightman, M., & Nandra, K. 2012, A&A, 546, A98
Akylas, A., Georgantopoulos, I., Ranalli, P., et al. 2016, A&A, 594, A73
Akylas, A., Georgantopoulos, I., Gandhi, P., Boorman, P., & Greenwell, C. L. 2024, A&A, 692, A250
Ananna, T. T., Treister, E., Urry, C. M., et al. 2019, ApJ, 871, 240
Ananna, T. T., Weigel, A. K., Trakhtenbrot, B., et al. 2022, ApJS, 261, 9
Arévalo, P., Bauer, F. E., Puccetti, S., et al. 2014, ApJ, 791, 81
Asmus, D., Greenwell, C. L., Gandhi, P., et al. 2020, MNRAS, 494, 1784
Avni, Y., & Bahcall, J. N. 1980, ApJ, 235, 694
Baloković, M., Comastri, A., Harrison, F. A., et al. 2014, ApJ, 794, 111
Baloković, M., García, J. A., & Cabral, S. E. 2019, RNAAS, 3, 173
Barger, A. J., Cowie, L. L., Mushotzky, R. F., et al. 2005, AJ, 129, 578
Barthelmy, S. D., Barbier, L. M., Cummings, J. R., et al. 2005, Space Sci. Rev., 120, 143
Baumgartner, W. H., Tueller, J., Markwardt, C. B., et al. 2013, ApJS, 207, 19
Boorman, P. G., Gandhi, P., Buchner, J., et al. 2024, ArXiv e-prints [arXiv:2410.07339]
Brightman, M., Nandra, K., Salvato, M., et al. 2014, MNRAS, 443, 1999
Buchner, J., & Bauer, F. E. 2017, MNRAS, 465, 4348
Buchner, J., Georgakakis, A., Nandra, K., et al. 2014, A&A, 564, A125
Buchner, J., Georgakakis, A., Nandra, K., et al. 2015, ApJ, 802, 89
Buchner, J., Brightman, M., Baloković, M., et al. 2021, A&A, 651, A58
Burlon, D., Ajello, M., Greiner, J., et al. 2011, ApJ, 728, 58
Carroll, C. M., Ananna, T. T., Hickox, R. C., et al. 2023, ApJ, 950, 127
Churazov, E., Sunyaev, R., Revnivtsev, M., et al. 2007, A&A, 467, 529
Civano, F., Hickox, R. C., Puccetti, S., et al. 2015, ApJ, 808, 185
Comastri, A., Setti, G., Zamorani, G., & Hasinger, G. 1995, A&A, 296, 1
Comastri, A., Gilli, R., Marconi, A., Risaliti, G., & Salvati, M. 2015, A&A, 574, L10
Corral, A., Georgantopoulos, I., Akylas, A., & Ranalli, P. 2019, A&A, 629, A133
Fotopoulou, S., Buchner, J., Georgantopoulos, I., et al. 2016, A&A, 587, 16
Frontera, F., Orlandini, M., Landi, R., et al. 2007, ApJ, 666, 86
García-Burillo, S., Combes, F., Ramos Almeida, C., et al. 2016, ApJ, 823, L12
Gehrels, N., Chincarini, G., Giommi, P., et al. 2004, ApJ, 611, 1005
Georgakakis, A., Aird, J., Schulze, A., et al. 2017, MNRAS, 471, 1976
Georgakakis, A., Ruiz, A., & LaMassa, S. 2020, MNRAS, 499, 710
Georgantopoulos, I., & Akylas, A. 2019, A&A, 621, A28
Georgantopoulos, I., Akylas, A., Georgakakis, A., & Rowan-Robinson, M. 2009, A&A, 507, 747
Georgantopoulos, I., Comastri, A., Vignali, C., et al. 2013, A&A, 555, A43
Giacconi, R., Gursky, H., Paolini, F. R., & Rossi, B. B. 1962, Phys. Rev. Lett., 9, 439
Gilli, R., Comastri, A., & Hasinger, G. 2007, A&A, 463, 79
Gilli, R., Norman, C., Calura, F., et al. 2022, A&A, 666, A17

Greenwell, C. L., Klindt, L., Lansbury, G. B., et al. 2024, ApJS, 273, 20
Harrison, F. A., Craig, W. W., Christensen, F. E., et al. 2013, ApJ, 770, 103
Hickox, R. C., Myers, A. D., Greene, J. E., et al. 2017, ApJ, 849, 53
Ho, L. C., Filippenko, A. V., & Sargent, W. L. W. 1997, ApJ, 487, 568
Hönig, S. F., Kishimoto, M., Antonucci, R., et al. 2012, ApJ, 755, 149
Jana, A., Naik, S., & Kumari, N. 2022, JA&A, 43, 4
Koss, M. J., Assef, R., Baloković, M., et al. 2016, ApJ, 825, 85
Koss, M. J., Ricci, C., Trakhtenbrot, B., et al. 2022, ApJS, 261, 2
Koulouridis, E., Georgantopoulos, I., Loukaidou, G., et al. 2016, A&A, 586, A3
Laloux, B., Georgakakis, A., Andonie, C., et al. 2023, MNRAS, 518, 2546
Lansbury, G. B., Alexander, D. M., Aird, J., et al. 2017a, ApJ, 846, 20
Lansbury, G. B., Stern, D., Aird, J., et al. 2017b, ApJ, 836, 99
Lanzuisi, G., Ranalli, P., Georgantopoulos, I., et al. 2015, A&A, 573, A137
Lanzuisi, G., Delvecchio, I., Berta, S., et al. 2017, A&A, 602, A123
Loredo, T. J. 2004, in American Institute of Physics Conference Series, eds. R. Fischer, R. Press, & U. V. Toussaint, 735, 195
Lynden-Bell, D. 1969, Nature, 223, 690
Maccacaro, T., Gioia, I. M., & Stocke, J. T. 1984, ApJ, 283, 486
Marchesi, S., Ajello, M., Comastri, A., et al. 2017, ApJ, 836, 116
Marchesi, S., Ajello, M., Marcotulli, L., et al. 2018, ApJ, 854, 49
Marchesi, S., Ajello, M., Zhao, X., et al. 2019, ApJ, 882, 162
Marinucci, A., Bianchi, S., Matt, G., et al. 2016, MNRAS, 456, L94
Mateos, S., Warwick, R. S., Carrera, F. J., et al. 2008, A&A, 492, 51
Miyaji, T., Hasinger, G., Salvato, M., et al. 2015, ApJ, 804, 104
Murphy, K. D., & Yaqoob, T. 2009, MNRAS, 397, 1549
Mushotzky, R. F., Cowie, L. L., Barger, A. J., & Arnaud, K. A. 2000, Nature, 404, 459
Nenkova, M., Sirocky, M. M., Ivezić, Ž., & Elitzur, M. 2008, ApJ, 685, 147
Oda, S., Tanimoto, A., Ueda, Y., et al. 2017, ApJ, 835, 179
Page, M. J., & Carrera, F. J. 2000, MNRAS, 311, 433
Panagiotou, C., Walter, R., & Paltani, S. 2021, A&A, 653, A162
Possolo, A., Merkatas, C., & Bodnar, O. 2019, Metrologia, 56, 045009
Pouliasis, E., Ruiz, A., Georgantopoulos, I., et al. 2024, A&A, 685, A97
Press, W. H., Teukolsky, S. A., Vetterling, W. T., & Flannery, B. P. 1992, Numerical recipes in FORTRAN. The art of scientific computing (Cambridge: University Press)
Puccetti, S., Comastri, A., Fiore, F., et al. 2014, ApJ, 793, 26
Ranalli, P., Koulouridis, E., Georgantopoulos, I., et al. 2016, A&A, 590, A80
Revnivtsev, M., Gilfanov, M., Sunyaev, R., Jahoda, K., & Markwardt, C. 2003, A&A, 411, 329
Ricci, C., Ueda, Y., Koss, M. J., et al. 2015, ApJ, 815, L13
Ricci, C., Trakhtenbrot, B., Koss, M. J., et al. 2017, Nature, 549, 488
Saha, T., Markowitz, A. G., & Buchner, J. 2022, MNRAS, 509, 5485
Sakamoto, K., Aalto, S., Evans, A. S., Wiedner, M. C., & Wilner, D. J. 2010, ApJ, 725, L228
Schmidt, M. 1968, ApJ, 151, 393
Semena, A. N., Sazonov, S. Y., & Krivonos, R. A. 2019, Astron. Lett., 45, 490
Sengupta, D., Marchesi, S., Vignali, C., et al. 2023, A&A, 676, A103
Silver, R., Torres-Albà, N., Zhao, X., et al. 2022, ApJ, 940, 148
Tanimoto, A., Ueda, Y., Odaka, H., et al. 2019, ApJ, 877, 95
Tanimoto, A., Ueda, Y., Odaka, H., Yamada, S., & Ricci, C. 2022, ApJS, 260, 30
Titarchuk, L. 1994, ApJ, 434, 570
Torres-Albà, N., Marchesi, S., Zhao, X., et al. 2021, ApJ, 922, 252
Traina, A., Marchesi, S., Vignali, C., et al. 2021, ApJ, 922, 159
Treister, E., Urry, C. M., & Virani, S. 2009, ApJ, 696, 110
Ueda, Y., Akiyama, M., Hasinger, G., Miyaji, T., & Watson, M. G. 2014, ApJ, 786, 104
Yamada, S., Ueda, Y., Tanimoto, A., et al. 2021, ApJS, 257, 61
Zaino, A., Bianchi, S., Marinucci, A., et al. 2020, MNRAS, 492, 3872
Zhao, X., Marchesi, S., Ajello, M., Baloković, M., & Fischer, T. 2020, ApJ, 894, 71
Zhao, X., Marchesi, S., Ajello, M., et al. 2021, A&A, 650, A57

Appendix A: The Compton-thick active galactic nuclei

Table A.1. The Compton-thick AGN sample.

Name (1)	α (2)	δ (3)	redshift (4)	$F_{14-195\,keV}$ (5)	N_H (6)	log $L_{10-50\,keV}$ (7)	Ref. (8)	Sample (9)
2MASX J00253292+6821442	00:25:33	+68:21:44	0.012	18^{+5}_{-4}	$3.20^{+0.35}_{-0.30}$	$43.06^{+0.11}_{-0.12}$	g,h	3
MCG -07-03-007	01:05:27	-42:12:58	0.02988	12 ± 4	$0.90^{+0.11}_{-0.09}$	$43.39^{+0.13}_{-0.17}$	f,a	1
2MASX J01073963-113912	01:07:40	-11:39:12	0.04746	10^{+-10}_{-10}	$3.00^{+100.00}_{-0.05}$	$43.78^{+0.99}_{-0.56}$	e	2
NGC 0424	01:11:28	-38:05:01	0.01176	21 ± 4	3.20 ± 0.19	$43.09^{+0.08}_{-0.09}$	c,e,a,b	1
NGC 612	01:33:58	-36:29:36	0.0298	55^{+5}_{-4}	0.90 ± 0.10	44.05 ± 0.04	e	4
NGC 1068	02:42:41	-00:00:48	0.0038	35 ± 4	$10.00^{+100.00}_{-0.80}$	$43.06^{+0.37}_{-0.27}$	c,r,b,l	1
NGC 1106	02:50:41	+41:40:17	0.01447	19 ± 5	$4.80^{+100.00}_{-0.20}$	$43.60^{+0.75}_{-0.27}$	a,p	1
2MFGC 02280	02:50:43	+54:42:18	0.01515	27 ± 5	$2.00^{+2.17}_{-0.20}$	$43.34^{+0.19}_{-0.11}$	a,b,h	1
NGC 1125	02:51:40	-16:39:04	0.01093	17 ± 4	$1.30^{+0.70}_{-0.30}$	$42.74^{+0.12}_{-0.13}$	c,a,e	1
NGC 1142	02:55:12	-00:11:01	0.02885	88 ± 5	1.60 ± 0.30	44.33 ± 0.05	e,c	4
NGC 1194	03:03:49	-01:06:13	0.0136	37 ± 5	1.00 ± 0.10	$43.20^{+0.05}_{-0.06}$	e,c,b,a,g	1
ESO201-4	03:50:24	-50:18:35	0.0359	21 ± 4	$2.20^{+0.50}_{-0.60}$	$43.98^{+0.10}_{-0.11}$	e	4
CGCG 420-015	04:53:26	+04:03:42	0.02939	28 ± 5	$1.60^{+1.20}_{-1.30}$	$43.85^{+0.17}_{-0.20}$	c,a	1
ESO 005-G004	06:05:42	-86:37:55	0.0062	34^{+5}_{-4}	1.10 ± 0.20	$42.49^{+0.06}_{-0.07}$	c,a (*)	1
Mrk 3	06:15:36	+71:02:15	0.0135	141 ± 5	$0.87^{+0.13}_{-0.08}$	43.75 ± 0.02	e	2
ESO 426-G002	06:23:46	-32:13:00	0.0224	24 ± 4	1.00 ± 0.03	$43.46^{+0.07}_{-0.08}$	f	3
2MASX J06561197-4919499	06:56:12	-49:19:50	0.041	12 ± 4	$1.40^{+0.16}_{-0.09}$	$43.77^{+0.13}_{-0.16}$	a,f	2
MCG +06-16-028	07:14:04	+35:16:45	0.01569	17 ± 5	1.00 ± 0.17	$42.98^{+0.12}_{-0.15}$	c,a,d,h	1
NGC 2788A	09:02:39	-68:13:37	0.01335	20 ± 4	$2.31^{+0.52}_{-0.76}$	$43.10^{+0.11}_{-0.14}$	a,p	1
ESO 565-G019	09:34:44	-21:55:40	0.01629	21 ± 6	$3.00^{+0.90}_{-0.70}$	$43.36^{+0.15}_{-0.16}$	e,a,k	2
MCG +10-14-025	09:35:52	+61:21:11	0.03937	8^{+4}_{-3}	$1.50^{+0.53}_{-0.09}$	$43.57^{+0.15}_{-0.23}$	a,r	2
NGC 3079	10:01:58	+55:40:47	0.00372	33 ± 4	2.50 ± 0.23	$42.22^{+0.05}_{-0.06}$	c,a,b	1
ESO 317-G041	10:31:23	-42:03:38	0.01932	17 ± 4	$0.85^{+0.16}_{-0.12}$	$43.14^{+0.10}_{-0.13}$	a	1
NGC 3281	10:31:52	-34:51:13	0.01061	86 ± 5	2.00 ± 0.30	$43.49^{+0.04}_{-0.05}$	e,g	4
NGC 3393	10:48:23	-25:09:43	0.01251	26^{+6}_{-5}	$1.90^{+1.50}_{-0.40}$	$43.13^{+0.16}_{-0.13}$	c,a	1
NGC 4180	12:13:03	+07:02:20	0.00699	17 ± 5	$1.50^{+0.36}_{-0.24}$	$42.35^{+0.12}_{-0.15}$	e,a,p	1
ESO 323-G032	12:53:20	-41:38:08	0.016	15^{+6}_{-5}	$1.80^{+1.46}_{-0.49}$	$43.10^{+0.19}_{-0.21}$	f,a	2
NGC 4941	13:04:13	-05:33:06	0.0037	20 ± 5	3.10 ± 1.70	$42.06^{+0.19}_{-0.21}$	b,j	3
NGC 4945	13:05:27	-49:28:06	0.01932	285 ± 6	3.80 ± 0.16	44.74 ± 0.02	c,a,o	1
Circinus	14:13:10	-65:20:21	0.0014	272 ± 4	$7.00^{+3.00}_{-2.00}$	$42.69^{+0.20}_{-0.17}$	n,b	1
NGC 5643	14:32:41	-44:10:28	0.004	18^{+6}_{-5}	$1.60^{+0.40}_{-0.30}$	$41.90^{+0.13}_{-0.16}$	c,a,b	1
NGC 5728	14:42:24	-17:15:11	0.00935	89 ± 6	$1.20^{+0.11}_{-0.04}$	43.28 ± 0.03	a,b,c	1
CGCG 164-019	14:45:37	+27:02:05	0.0299	14^{+5}_{-4}	$1.20^{+0.50}_{-0.36}$	$43.51^{+0.14}_{-0.17}$	c,a,h	1
ESO 137-G034	16:35:14	-58:04:48	0.00914	28^{+6}_{-5}	2.90 ± 0.20	$42.97^{+0.08}_{-0.10}$	a,b	1
NGC 6232	16:43:20	+70:37:57	0.0148	12 ± 4	$0.57^{+0.70}_{-0.10}$	$42.72^{+0.15}_{-0.18}$	e,a,b	1
NGC 6240	16:52:59	+02:24:03	0.02448	72 ± 6	1.20 ± 0.14	44.04 ± 0.04	e,a	1
NGC 6552	18:00:07	+66:36:54	0.02649	19 ± 4	$2.20^{+0.40}_{-0.31}$	$43.68^{+0.09}_{-0.11}$	f,a	1
NGC 6921	20:28:29	+25:43:24	0.0145	78 ± 5	1.70 ± 0.30	43.68 ± 0.05	m,h	1
ESO 464-G016	21:02:24	-28:10:29	0.03635	17^{+6}_{-5}	$0.86^{+0.17}_{-0.16}$	$43.72^{+0.13}_{-0.16}$	e,a	2
NGC 7130	21:48:20	-34:57:04	0.01615	16^{+6}_{-5}	$3.40^{+0.50}_{-0.40}$	$43.30^{+0.14}_{-0.19}$	e,a,b	1
NGC 7212	22:07:01	+10:13:52	0.02667	11^{+5}_{-4}	$1.90^{+0.50}_{-0.40}$	$43.42^{+0.16}_{-0.22}$	c,a	1
NGC 7479	23:04:57	+12:19:22	0.00794	20 ± 5	6.10 ± 0.90	$43.00^{+0.12}_{-0.14}$	c,a,d	1
CGCG 475-040	23:07:49	+22:42:37	0.03473	14^{+5}_{-4}	$1.60^{+0.23}_{-0.15}$	$43.71^{+0.12}_{-0.17}$	f,a	2
NGC 7582	23:18:24	-42:22:14	0.0053	81 ± 4	$1.70^{+0.10}_{-0.15}$	42.81 ± 0.03	c,a,e	1

Notes. Column Description: (1) Name (2) Right Ascension (3) Declination (4) Redshift (5) Observed flux (14-195 keV) from BAT catalogue in units of 10^{-12} ergs sec^{-1} cm^{-2} (6) Hydrogen column density in units of 10^{24} cm^{-2} (7) log Luminosity (10-50 keV) (8) References: a. Tanimoto et al. (2022) b. Georgantopoulos & Akylas (2019) c. Marchesi et al. (2018) d.Marchesi et al. (2019) e. Zhao et al. (2021) f. Torres-Albà et al. (2021) g. Semena et al. (2019) h. Koss et al. (2016) i. Panagiotou et al. (2021) j. Jana et al. (2022) k. Traina et al. (2021) l. Zaino et al. (2020) m. Yamada et al. (2021) n. Arévalo et al. (2014) o. Puccetti et al. (2014) p. Sengupta et al. (2023) q. Marinucci et al. (2016) r. Oda et al. (2017) s. Zhao et al. (2020) (9) Parent sample: 1. Common in Ricci et al. (2015) and Akylas et al. (2016); 2. Only in Ricci et al. (2015); 3. Only in Akylas et al. (2016) 4. Zhao et al. (2021)